Molecular Engineering to Tune the Ligand Environment of Atomically Dispersed Nickel for Efficient Alcohol Electrochemical Oxidation

Zhifu Liang+, Daochuan Jiang+, Xiang Wang, Mohsen Shakouri, Ting Zhang, Zhongjun Li, Pengyi Tang*, Jordi Llorca, Lijia Liu*, Yupeng Yuan, Marc Heggen, Rafal E. DuninBorkowski, Joan R. Morante, Andreu Cabot*, Jordi Arbiol*

Z. F Liang, T. Zhang, Prof. J. Arbiol Catalan Institute of Nanoscience and Nanotechnology (ICN2), CSIC and BIST Campus UAB, Bellaterra, 08193 Barcelona, Catalonia, Spain Email: arbiol@icrea.cat

Dr. P. Y Tang Shanghai Institute of Microsystem and Information Technology, Chinese Academy of Sciences, Shanghai 200050, China Email: py.tang@mail.sim.ac.cn

Dr. D. Jiang, Prof. Y. Yuan School of Chemistry and Chemical Engineering, Anhui University, Heifei 230601, Anhui Province, China

Z.F Liang, X. Wang, Prof. J. R. Morante, Prof. A. Cabot Catalonia Institute for Energy Research - IREC Sant Adrià de Besòs, Barcelona, 08930, Catalonia, Spain Email: acabot@irec.cat

Dr. L. Liu Department of Chemistry, Western University, 1151 Richmond Street, London, ON N6A5B7 Canada Email: lijia.liu@uwo.ca

Dr. P. Y Tang, Dr. M Heggen, Prof. R E. Dunin-Borkowski Ernst Ruska-Centre for Microscopy and Spectroscopy with Electrons and Peter Grünberg Institute Forschungszentrum Jülich GmbH 52425 Jülich, Germany

Prof. Z.J Li School of Physics, Hefei University of Technology, Hefei 230009, P. R China

Dr. M. Shakouri Canadian Light Source, Saskatoon, S7N 0X4, Canada

Prof. J. Llorca Institute of Energy Technologies, Department of Chemical Engineering and Barcelona Research Center in Multiscale Science and Engineering Universitat Politècnica de Catalunya, EEBE, 08019 Barcelona, Catalonia Spain.

Prof. A. Cabot, Prof. J. Arbiol ICREA Pg. Lluís Companys 23, 08010 Barcelona, Catalonia, Spain

+ These authors contributed equally to this work

* Corresponding authors

Abstract

Atomically dispersed metals maximize the number of catalytic sites and enhance their activity. However, their challenging synthesis and characterization strongly complicates their optimization. Here, the aim is to demonstrate that tuning the electronic environment of atomically dispersed metal catalysts through the modification of their edge coordination is an effective strategy to maximize their performance. This article focuses on

optimizing nickel-based electrocatalysts toward alcohol electrooxidation in alkaline solution. A new organic framework with atomically dispersed nickel is first developed. The coordination environment of nickel within this framework is modified through the addition of carbonyl (C☐O) groups. The authors then demonstrate that such nickel-based organic frameworks, combined with carbon nanotubes, exhibit outstanding catalytic activity and durability toward the oxidation of methanol (CH_3OH), ethanol (CH_3CH_2OH), and benzyl alcohol ($C_6H_5CH_2OH$); the smaller molecule exhibits higher catalytic performance. These outstanding electrocatalytic activities for alcohol electrooxidation are attributed to the presence of the carbonyl group in the ligand chemical environment, which enhances the adsorption for alcohol, as revealed by density functional theory calculations. The work not only introduces a new atomically dispersed Ni-based catalyst, but also demonstrates a new strategy for designing and engineering high-performance catalysts through the tuning of their chemical environment.

1 Introduction

The electrochemical oxidation of alcohols is at the basis of several strategic chemical processes and energy technologies, including electrochemical organic synthesis, biomass, and organic waste valorization, and direct alcohol fuel cells (DAFC).[1] The electrooxidation of alcohols offer numerous advantages over competing valorization strategies and energy technologies, such as high energy densities and energy conversion efficiency, operation/reaction at low working temperature with high selectivity, and low fuel cost with easy production, transportation, and storage.[1] However, despite their numerous advantages, the deployment of electrocatalytic valorization strategies and DAFCs is hampered by their low cost-effectiveness in large part associated with the use of moderately efficient catalysts based on high-cost and low-abundance elements such as platinum and palladium.[2, 3] Besides, current alcohol electrooxidation catalysts become rapidly poisoned with carbon monoxide, which further limits their cost-effectiveness. Thus, the development of efficient and stable alcohol oxidation electrocatalysts based on abundant elements is a topic of major interest.

Several non-precious transition metal catalysts have been proposed for alcohol electro-oxidation.[4, 5] Among them, nickel-based catalysts are considered the most promising candidates owing to their high catalytic activity, low price, and notable abundance. Numerous Ni-based catalysts, such as $Ni_{0.75}Cu_{0.25}$,[6] NiSn alloy,[7] $Ni_{93}Bi_7$,[8] NiSe,[9] NiO,[10] and metal–organic frameworks with

Ni(OH)$_4$,[11] and Ni-Co hydroxide[12] have been developed and tested for alcohol electrochemical-oxidation. However, the reported onset potentials and stabilities are still not fully satisfactory, which calls for novel strategies to design and engineer nickel-based catalysts with improved performance.

Recently, 2D covalent organic frameworks and metal–organic frameworks (MOF) with highly tunable pore structure and functionality, and high density of active sites, have arisen broad interest as electrocatalysts.[13] Optimized electrocatalysts based on such 2D structures have demonstrated outstanding performances toward oxygen evolution and reduction,[14, 15] and carbon dioxide reduction.[16, 17] However, despite their high potential for alcohol electrooxidation, these 2D materials and particularly a nickel-containing 2D organic framework have yet to be developed and optimized toward this electrocatalytic reaction.

Here, we report the synthesis of an atomically-dispersed nickel 2D molecular organic framework containing abundant carbonyl (C▢O) functional groups within the nickel ion coordination environment. Its atomic structure and how the outstanding electrocatalytic activities and durabilities obtained for the electrochemical-oxidation of methanol, ethanol, and benzyl alcohol were analyzed, are related to the alcohol adsorption ability of the carbonyl functional groups and the high unsaturated coordination number of the nickel ions within the new catalyst presented here.

2 Results and Discussion

The nickel-based 2D organic framework with abundant carbonyl functional groups (Ni–2D–O–SA) was solvothermally synthesized through a Schiff-based reaction between 2,5-hydroxyterephthalaldehyde (HBC) (Scheme **S1**, Supporting Information) and tetramino-benzoquinone (TABQ) (Scheme **S2**, Supporting Information) in *N*-methyl-2-pyrrolidone (NMP) (see details in **Figure 1a**; Scheme **S3**, Supporting Information). The dark-black color of the obtained solid indicated the formation of a conjugated polymer, which was washed by water and methanol to remove low molecular mass impurities, and then dried under vacuum. For comparison, a reference nickel-based 2D organic framework without carbonyl chemical groups (Ni–2D–SA) was prepared under the same reaction condition but using 1,2,4,5-benzenetetraamine tetrahydrochloride (TAB) instead of TABQ (Scheme **S4**, Supporting Information).[18]
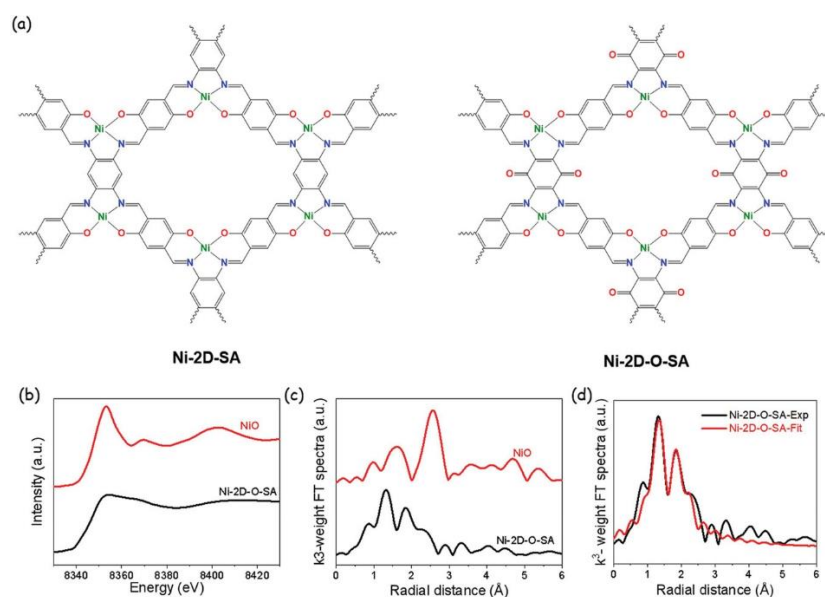
Figure 1 a) Scheme of the synthesis procedure used to produce Ni–2D–O–SA. b) Ni K-edge XANES spectrum of Ni–2D–O–SA compared with a commercial NiO powder. c) Fourier transformed Ni K-edge EXAFS spectra of Ni–2D–O–SA and NiO plotted in R-space. d) Fitting of the Fourier transformed EXAFS spectrum in R-space of Ni–2D–O–SA.

Scanning electron microscopy (SEM) images (Figure **S1a,b**, Supporting Information) show that the Ni–2D–O–SA sample has a cotton-like morphology. The X-ray diffraction (XRD) pattern (Figure **S3**, Supporting Information) of the Ni–2D–O–SA powder was similar to that of graphite, with a diffraction peak at 26.29° corresponding to the (001) family planes and which indicated π–π layered stacking.[19] In contrast to the clear crystalline and layered structure displayed by Ni–2D–O–SA, the XRD pattern of Ni–D–SA displayed a much broader and less intense peak at around 26°. This result indicates that the introduction of carbonyl groups enhances the crystallinity of the nickel-based 2D organic framework used here.

Fourier transform infrared (FT-IR) spectroscopy was used to evaluate the chemical structure of the samples (Figure **S4**, Supporting Information). Based on the FT-IR spectra, the signal for C☐N appeared at 1642 cm⁻¹ for Ni–2D–SA, and 1648 cm⁻¹ for Ni–2D–O–SA. The vibration of the carbonyl bond (C☐O) in Ni–2D–O–SA negatively shifted below 1600 cm⁻¹ and overlapped with other vibrations. For Ni–2D–O–SA, the vibration peak for the C☐(C☐O)☐C bond, which is a footprint of TABQ, shifted from 1140 to 1010 cm⁻¹ due to the coordination effect and the attraction between the layers. This result already points out to the successful introduction of the carbonyl groups in the organic framework.[20]

The survey X-ray photoelectron spectroscopy (XPS) spectra revealed the sole presence of C, N, Ni, and O in both samples (Figures **S5** and **S6**, Supporting Information).[21] For both samples, the high-resolution Ni 2p spectrum showed a unique doublet at binding energies of 856 eV (Ni $2p_{3/2}$) and 873.3 eV (Ni $2p_{1/2}$), significantly above those of NiO.[22, 23]

The local environment in Ni–2D–O–SA was further analyzed and compared with that of NiO using X-ray absorption fine structure (XAFS) at the Ni K-edge (Figure **1b–d**; Figure **S7**, Supporting Information). Comparing the spectral features at the near-edge, that is, the X-ray absorption near-edge structure (XANES), we observe the absorption onset of Ni–2D–O–SA at slightly lower energy than that of NiO (Figure **1b**). Differences are more clearly seen when plotting the first derivative of the two spectras (Figure **S7a**, Supporting Information), as shown in the inset of **Figure 2b**. Besides, the main absorption peak of Ni–2D–O–SA has a lower intensity than that of NiO. Both features indicate that compared with NiO, where Ni is fully surrounded by O, within Ni–2D–O–SA, Ni atoms are partially surrounded by a lower electronegativity element, that is, N. A more quantitative picture was obtained by analyzing the extended XAFS (EXAFS) features. The fitting of the Fourier transformed EXAFS spectrum suggests that Ni is coordinated with two N atoms and two O atoms, at a bond length 1.87 and 2.05 Å, respectively (Figure **1c,d**).[24] The contribution at longer radial distances comes from C atoms with a coordination number of 6 and a bond length of 2.65 Å. The detailed fitting parameters can be found in Table **S1**, Supporting Information. Overall, XAFS analysis provided strong evidence of the formation of the NiN_2O_2 salophen structure unit in the Ni–2D–O–SA framework.
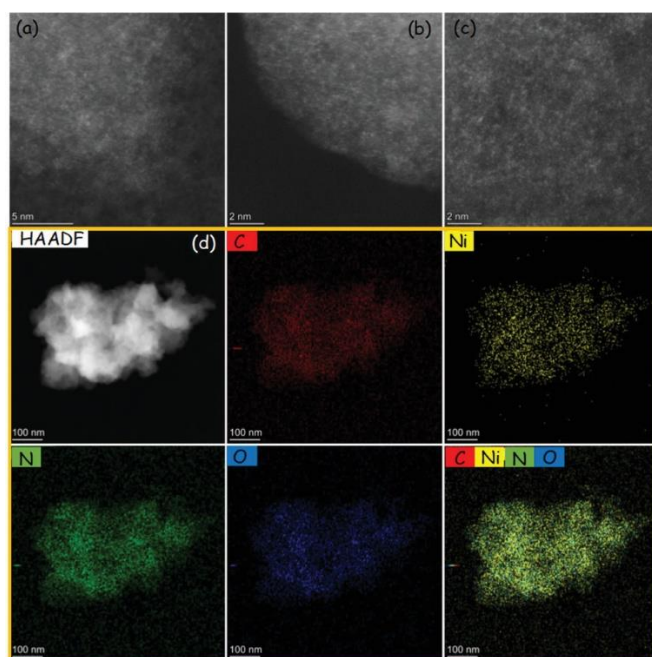
Figure 2 a–c) HAADF–STEM images of Ni–2D–O–SA displaying the presence of atomically dispersed nickel atoms. d) Low magnification HAADF–STEM image and EDS elemental mapping.

High angle annular dark-field (HAADF) aberration-corrected scanning transmission electron microscopy (STEM) was used to analyse the nickel dispersion. As shown in Figure **2a–c**; Figure **S8a–c**, Supporting Information, Ni–2D–O–SA contained a high density of isolated and homogeneously distributed nickel atoms. The uniform distribution of Ni, C, N, and O was further confirmed by energy-dispersed X-ray spectroscopy (EDS) elemental mapping (Figure **2d**).

The surface area of Ni–2D–O–SA and Ni–2D–SA, evaluated from N_2 adsorption–desorption isotherms at 77 K (Figure **S9**, Supporting Information) using the Brunauer–Emmett–Teller equation was 21.1 and 83 m^2 g^{-1}, respectively. Thus, the introduction of carbonyl functional groups significantly decreased the surface area of the material, which we associate with an enhancement of the layer–layer interaction that results in slightly more densely packed frameworks.

To improve the electrical conductivity of these nickel-based organic frameworks, as required to apply them as electrocatalysts, they were loaded on multi-wall carbon nanotubes (CNT) through the π–π packing interaction. The XRD patterns of the obtained Ni–2D–O–SA–CNT and Ni–2D–SA–CNT composites, showed a unique peak at ≈26° (Figure **S10**, Supporting Information), which was assigned to the overlap between the CNT and the organic framework structures. SEM (Figure **S1c,d**, Supporting Information), STEM images, and EDX compositional maps (Figure **S11**, Supporting Information) showed the composites morphology and confirmed the homogeneous loading of Ni–2D–O–SA on the CNTs.

Figure 3a exhibits the cyclic voltammograms (CV) of the two samples in the range from 0 to 0.65 V in 1.0 M KOH electrolyte with a scan rate of 50 mV s^{-1}. The anodic peak at 0.50 V versus Hg/HgO measured in the forward scan with Ni–2D–O–SA–CNT is attributed to Ni^{2+} oxidation, and the cathodic peak in the backward scan at 0.38 V corresponds to the reduction of Ni^{3+} species. For Ni–2D–SA–CNT, the anodic peak shifted to 0.54 V and the cathodic peak to 0.42 V. The current density at the Ni^{2+} oxidation peak in the Ni–2D–O–SA–CNT electrocatalyst was 19 mA cm^{-2}, which is ≈9.5 times higher than that of Ni–2D–SA–CNT, 2 mA cm^{-2}. These results indicate a much higher electrochemical activity of the Ni ions within Ni–2D–O–SA–CNT and their easier oxidation to Ni^{3+}. Besides, the ratio between the anodic and the cathodic

peak current densities was close to 1 for both catalysts, indicating a reversible Ni^{2+}/Ni^{3+} redox reaction in both materials.[25]
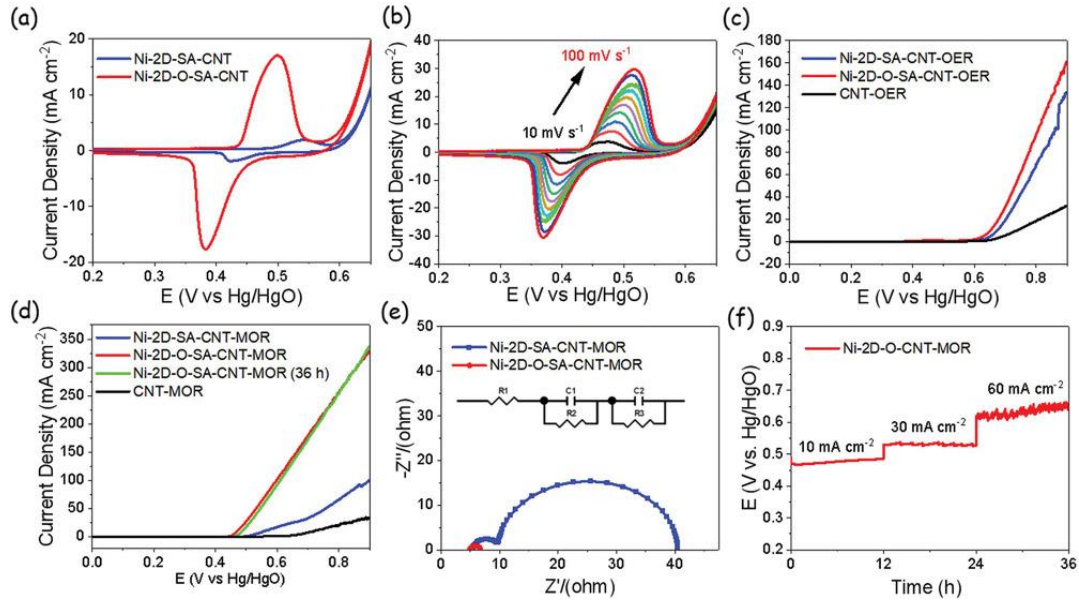
Figure 3 a) CV of Ni–2D–O–SA–CNT and Ni–2D–SA–CNT electrocatalysts in 1 M KOH at 50 mV s⁻¹ potential sweep rate. b) CVs of Ni–2D–O–SA–CNT electrocatalysts in 1 M KOH obtained at an increasing potential sweep rate, from 10 to 100 mV s⁻¹. c,d) LSV curves obtained with Ni–2D–SA–CNT, Ni–2D–O–SA–CNT, and reference carbon nanotubes (CNTs) catalysts in 1.0 M KOH (c) and 1 M KOH + 1 M methanol in the potential range 0 to 0.9 V versus Hg/HgO at a scan rate of 5 mV s⁻¹ (d). e) EIS Nyquist plots at 0.56 V in 1 M KOH + 1 M methanol solution. f) CP long-term stability of Ni–2D–O–SA–CNT at 10, 30, and 60 mA cm⁻². No iR compensation was applied to the displayed data.

CV of the reduction/oxidation process allowed to estimate the surface coverage (Γ) of Ni^{2+}/Ni^{3+} within Ni–2D–O–SA–CNT to be 1.32×10^{-7} mol cm⁻², two orders of magnitude above that of Ni–2D–SA–CNT, 5.17×10^{-9} mol cm⁻² (Figure **3a**; Equation (**S1**), Supporting information).[26] Figure **3b**; Figure **S12**, Supporting Information, display CV curves at different scan rates, from 10 to 100 mV s⁻¹, obtained with these two catalysts in 1.0 M KOH electrolyte. The variation of the anodic and cathodic peak current densities with the square root of the voltage scan rate was linearly fitted with $R^2 > 0.99$ for both samples (Figure **S12**, Supporting Information), demonstrating the Ni^{2+}/Ni^{3+} redox reaction to be diffusion limited.[25] From this dependence, an apparent diffusion coefficient D' was evaluated (see Equation **S3**, Supporting Information). The D' obtained with Ni–2D–O–SA–CNT is 2.3×10^{-6} g cm⁻¹ s⁻¹, which is close to an order of magnitude higher than with Ni–2D–SA–CNT, 3.3×10^{-7} g cm⁻¹ s⁻¹.

The alcohol electrooxidation performance of Ni–2D–O–SA–CNT and Ni–2D–SA–CNT electrocatalysts was analyzed by linear sweep voltammetry (LSV) in 1 M KOH and 1 M KOH + 1 M methanol solutions using a conventional three-electrode setup (Figure **3c,d**). The OER activity of Ni–2D–O–SA–CNT was just slightly improved compared to that of Ni–2D–SA–CNT. However, the Ni–2D–O–SA–CNT catalysts showed much higher activity toward methanol oxidation reaction (MOR), with current densities increasing from 31 to 106 mA cm^{-2} in the range 0.5–0.6 V versus Hg/HgO, that is, six-fold higher current densities compared with Ni–2D–SA–CNT. Thus, the introduction of the carbonyl group (C O) at the ligand environment of the dispersed Ni-atoms active sites clearly results in much higher MOR catalytic activities.

The charge transfer resistances of these two catalysts were evaluated through electrochemical impedance spectroscopy (EIS). The EIS Nyquist plot of Ni–2D–O–SA–CNT (Figure **3e**) presents a smaller semicircle than Ni–2D–SA–CNT at 0.56 V in 1 M KOH + 1 M methanol electrolyte, denoting a lower charge transfer resistance (R_3) and thus faster MOR kinetics.[27] On the other hand, the charge transfer resistance for OER of Ni–2D–O–SA–CNT is similar to that of Ni–2D–SA–CNT at 0.67 V (Figure **S13**, Supporting Information), which is consistent with the similar OER activities of these two catalysts.

As shown in the chronopotentiometry (CP) curve (Figure **3f**), the Ni–2D–O–SA–CNT electrocatalyst maintained constant current densities of 10 and 30 mA cm^{-2} for 12 h without a significant increase in the required potential. When increasing the current density to 60 mA cm^{-2}, the potential raised ≈4.8% during 12 h, which is attributed to the methanol consumption. After 36 h chronopotentiometry test, LSV curves recorded with the used electrocatalysts in a fresh 1 M KOH + 1 M methanol electrolyte (Figure **3d**) showed almost no variation with respect to those obtained with the fresh electrocatalysts, what demonstrates the excellent stability of Ni–2D–O–SA–CNT during MOR. After the stability test, the pH value of the solution is 14.12, which is not a significant change compared to the initial solution (pH = 14).

The XRD pattern of Ni–2D–O–SA–CNT after MOR (Figure **S14**, Supporting Information) displayed no significant variation with respect to the sample before the electrochemical tests, which confirmed the excellent structural stability of the 2D material and the growth of no additional crystalline phase of the nickel or nickel oxide nanoparticles during the reaction, indicating there is no agglomeration of nickel atom active sites.

Methanol adsorption is the initial and a limiting step in MOR. To understand the contribution of C O groups to methanol adsorption, density functional theory (DFT)

calculations were carried out. Selected fragments were shown in Figure **S15**, Supporting Information. **Figure 4** shows the optimal methanol adsorption configurations on top of a Ni site in both Ni–2D–SA and Ni–2D–O–SA. The adsorption energy is −0.248 eV and −0.225 eV in Ni−2D−SA and Ni−2D−O−SA, respectively. The negative adsorption energies suggest that methanol adsorption is thermodynamically favored in both cases. Interestingly, the adsorption distance (d) between the O atom of methanol and Ni in Ni–2D–O–SA is 3.11 Å, which is shorter than in Ni–2D–SA (3.27 Å). Compared with Ni–2D–SA, the 10% lower adsorption energy and 5% shorter adsorption distance indicate a more effective adsorption of the methanol molecule on the surface of Ni–2D–O–SA. What is more, upon adsorption, the H☐O☐CH₃ angle in Ni–2D–O–SA increases from 108.25° to 109.04°, while the H☐O☐CH₃ angle in Ni–2D–SA remains almost unchanged after optimization. This result indicates that Ni–2D–O–SA can facilitate the activation of the methanol molecule. We also identify the O of the C☐O group as a methanol adsorption site. DFT calculations show that the methanol molecule tends to adsorb at such O site with the OH group in methanol parallel to the surface. The shortest distance between the methanol molecule and the surface is 1.87 Å, which is much smaller than in the Ni–2D–SA surface (2.5 Å). Thus, based on the DFT calculations, it is reasonable to conclude that the addition of carbonyl (C☐O) groups to the organic framework results in more effective adsorption as well as activation of the methanol molecule, which explains the higher activity of Ni–2D–O–SA toward MOR when compared with Ni–2D–SA.
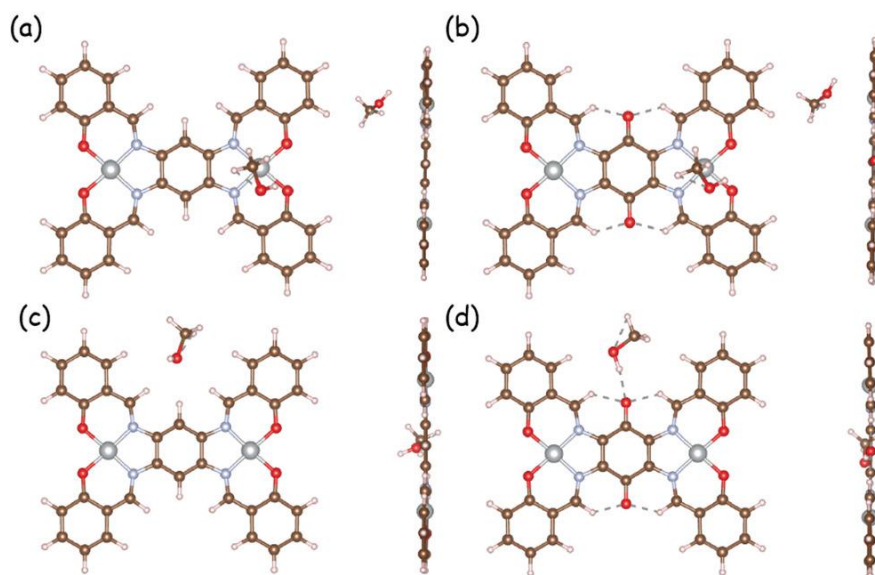

Figure 4 a,b) Optimal methanol adsorption configurations on top of the Ni site in both Ni–2D–SA (a) and Ni–2D–O–SA (b). c,d) Optimal methanol adsorption configurations on top of the carbonyl site in both Ni–2D–SA (c) and Ni–2D–O–SA (d) (red is oxygen, light blue is nitrogen, grey is nickel, brown is carbon).

Beyond MOR, we also examined the electrocatalytic activity of the produced catalysts toward the oxidation of other alcohols. Compared with Ni–2D–SA–CNT, Ni–2D–O–SA–CNT presented significantly higher electrocatalytic performance toward the electrochemical oxidation of both ethanol (EOR) (**Figure 5a**) and benzyl alcohol (BOR) (Figure **5b**). Especially for the BOR, the current density at 0.6 V obtained with Ni–2D–O–SA–CNT was ≈77 mA cm^{-2}, which is ≈eight times higher than that of Ni–2D–SA–CNT (9.7 mA cm^{-2}).
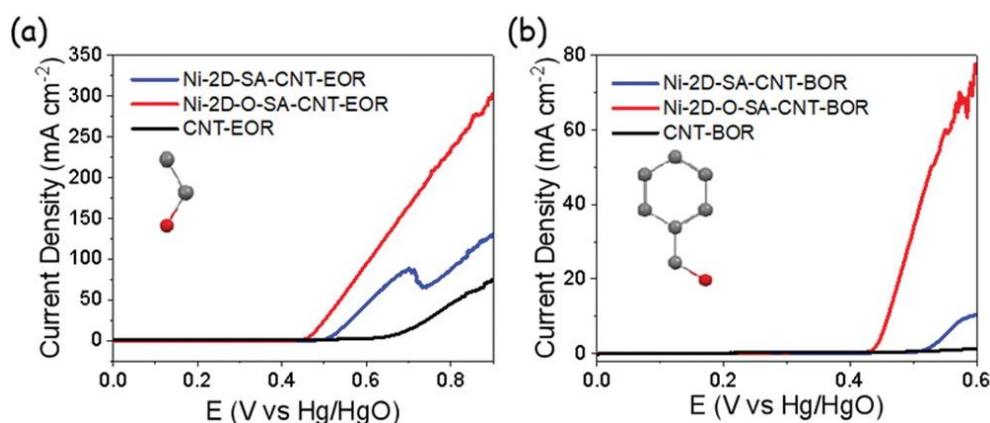
Figure 5 a) LSV of Ni–2D–SA–CNT, Ni–2D–O–SA–CNT, and CNT in 1 M KOH+1 M methanol from 0 to 0.9 V versus Hg/HgO at a scan rate of 5 mV s^{-1}. b) LSV of Ni–2D–SA–CNT, Ni–2D–O–SA–CNT, and the CNT in 1 M KOH + 0.1 M benzyl alcohol from 0 to 0.9 V versus Hg/HgO at a scan rate of 5 mV s^{-1}.

$$RCH_2OH \xrightarrow[\text{1 M KOH}]{\text{Electrocatalysts}} RCOO^-$$

$$R=H, CH_3, C_6H_5$$
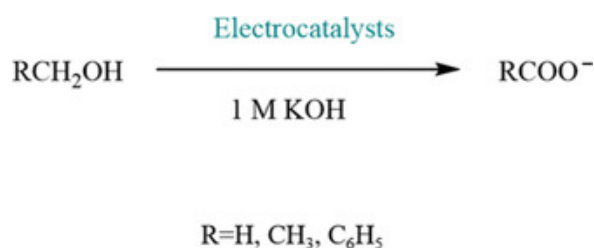
Figure 6 Scheme of the electrochemical oxidation reaction of alcohol. CP measurements were used to test the stability of Ni–2D–O–SA–CNT for EOR. As shown in Figure **S16**, Supporting Information, Ni–2D–SA–CNT exhibited excellent long-term stability for EOR, similar to that obtained for MOR. For BOR, chronoamperometric measurements (Figure **S17**, Supporting Information) show the current density decay associated with the consumption of benzyl alcohol. Notice in this respect that the initial concentration of benzyl alcohol was just 0.1 M, since the steric hindrance of benzene may prevent an efficient reaction at higher concentrations. The EIS spectra for EOR and BOR were similar to those obtained for MOR, confirming that Ni–2D–O–SA–CNT is also characterized by a highly efficient charge transfer and a highly favorable EOR and BOR kinetics (Figure **S18**, Supporting Information).

Finally, in order to confirm the product of the electrochemical oxidation of alcohol, nuclear magnetic resonance (NMR) tests were conducted to analyze the associated products of electrochemical oxidation of alcohol. As shown in Figure **S19**, Supporting Information, the NMR spectrum after the MOR stability test displays the characteristic chemical shift of HCOO⁻ at 8.33 ppm, while the characteristic chemical shift of HCHO in the range of ≈9–10 ppm was not observed, demonstrating that the final product of methanol oxidation is formate (HCOO⁻). Furthermore, the NMR spectrum (Figure **S20**, Supporting Information) of the products from benzyl alcohol oxidation showed a chemical shift in the range of ≈7–8 ppm, which is assigned to the characteristic chemical shift of the proton in the benzene ring of benzoate. The characteristic chemical shift belonging to the aldehyde (□CHO) of benzaldehyde was not observed at the range of ≈9–10 ppm, demonstrating that the final product of the benzyl alcohol oxidation was benzoate ($C_6H_5COO^-$). The NMR spectra of the EOR electrolyte did also not display the characteristic chemical shift of the aldehyde (□CHO). The characteristic chemical shift of CH_3COO^- appears at 1.83 ppm (Figure **S21**, Supporting Information).

Taking into account the above NMR results, we propose the following electrochemical reaction for the alcohol electrochemical oxidation (**Figure 6**):

3 Conclusion

In conclusion, we detailed the synthesis of a new nickel-based 2D organic framework and proposed a facile molecular engineering strategy to tune the ligand coordination environments of nickel ion centers. Through this strategy, carbonyl (C□O) groups were introduced and proved to decisively contribute to an efficient alcohol electro-oxidation in alkaline solution. EXAFS and XANES analysis confirmed the Ni salophen unit structure, NiN_2O_2, within the 2D organic frameworks. The atomically dispersed nickel within a framework containing the carbonyl groups displayed outstanding MOR, EOR, and BOR performance. DFT calculations suggested that the introduction of the C□O functional groups favor the absorption and activation of methanol molecules, which is at the origin of the improved MOR observed. The present work not only offers novel materials and a promising strategy to design more efficient atomically dispersed nickel-based catalysts for alcohol oxidation, but it could also benefit other research fields related to electrochemical-organic synthesis, energy conversion and storage.

Acknowledgements

REFERENCES

1 a) E. Antolini, E. R. Gonzalez, *J. Power Sources* 2010, **195**, 3431;

b) K. C. Cheung, W. L. Wong, D. L. Ma, T. S. Lai, K. Y. Wong, *Coord. Chem. Rev.* 2007, **251**, 2367;

c) D. P. Hickey, M. S. McCammant, F. Giroud, M. S. Sigman, S. D. Minteer, *J. Am. Chem. Soc.* 2014, **136**, 15917;

d) N. Kakati, J. Maiti, S. H. Lee, B. Viswanathan, Y. S. Yoon, *Chem. Rev.* 2014, **114**, 12397;

e) R. Ciriminna, G. Palmisano, M. Pagliaro, *ChemCatChem* 2015, **7**, 552.

2 Y. Tong, X. Yan, J. Liang, S. X. Dou, *Small* 2021, **17**, 1904126.

3 M. A. F. Akhairi, S. K. Kamarudin, *Int. J. Hydrogen Energy* 2016, **41**, 4214.

4 a) S. Rezaee, S. Shahrokhian, *Appl. Catal., B* 2019, **244**, 802;

b) A. Badalyan, S. S. Stahl, *Nature* 2016, **535**, 406.

5 G. M. K. Tolba, N. A. M. Barakat, A. M. Bastaweesy, E. A. Ashour, W. Abdelmoez, M. H. El-Newehy, S. S. Al-Deyab, H. Y. Kim, *J. Mater. Sci. Technol.* 2015, **31**, 97.

6 X. Cui, P. Xiao, J. Wang, M. Zhou, W. Guo, Y. Yang, Y. He, Z. Wang, Y. Yang, Y. Zhang, Z. Lin, *Angew. Chem., Int. Ed.* 2017, **56**, 4488.

7 J. Li, Z. Luo, Y. Zuo, J. Liu, T. Zhang, P. Tang, J. Arbiol, J. Llorca, A. Cabot, *Appl. Catal., B* 2018, **234**, 10.

8 A. Dubale, Y. Zheng, H. Wang, R. Hübner, Y. Li, J. Yang, J. Zhang, N. Sethi, L. He, Z. Zheng, W. Liu, *Angew. Chem., Int. Ed.* 2020, **132**, 13995.

9 B. Zhao, J. Liu, C. Xu, R. Feng, P. Sui, L. Wang, J. Zhang, J. L. Luo, X. Z. Fu, *Adv. Funct. Mater.* 2020, **31**, 2008812.

10 C. Liu, W. Zhou, J. Zhang, Z. Chen, S. Liu, Y. Zhang, J. Yang, L. Xu, W. Hu, Y. Chen, Y. Deng, *Adv. Energy Mater.* 2020, **10**, 2001397.

11 Y. Wu, J. Tian, S. Liu, B. Li, J. Zhao, L. Ma, D. Li, Y. Lan, X. Bu, *Angew. Chem., Int. Ed.* 2019, **58**, 12185.

12 H. Huang, C. Yu, X. Han, H. Huang, Q. Wei, W. Guo, Z. Wang, J. Qiu, *Energy Environ. Sci.* 2020, **13**, 4990.

13 X. Zhao, P. Pachfule, A. Thomas, *Chem. Soc. Rev.* 2021, **50**, 6871.

14 J. Du, F. Li, L.-C. Sun, *Chem. Soc. Rev.* 2021, **50**, 2663.

15 S. Royuela, E. Martinez-Perinan, M. P. Arrieta, J. I. Martinez, M. M. Ramos, F. Zamora, E. Lorenzo, J. L. Segura, *Chem. Commun.* 2020, **56**, 1267.

16 H. Zhu, M. Lu, Y. Wang, S. Yao, M. Zhang, Y. Kan, J. Liu, Y. Chen, S. Liu, Y. Lan, *Nat. Commun.* 2020, **11**, 497.

17 J. Liu, D. Yang, Y. Zhou, G. Zhang, G. Xing, Y. Liu, Y. Ma, O. Terasaki, S. Yang, L. Chen, *Angew. Chem., Int. Ed.* 2021, **60**, 14473.

18 T. Li, W.-D. Zhang, Y. Liu, Y. Li, C. Cheng, H. Zhu, X. Yan, Z. Li, Z.-G. Gu, *J. Mater. Chem. A* 2019, **7**, 19676.

19 B. P. Biswal, S. Chandra, S. Kandambeth, B. Lukose, T. Heine, R. Banerjee, *J. Am. Chem. Soc.* 2013, **135**, 5328.

20 L. Wang, Y. Ni, X. Hou, L. Chen, F. Li, J. Chen, *Angew. Chem., Int. Ed.* 2020, **59**, 22126.

21 Y. Liao, H. Wang, M. Zhu, A. Thomas, *Adv. Mater.* 2018, **30**, 1705710.

22 F. L. Li, Q. Shao, X. Huang, J. P. Lang, *Angew. Chem., Int. Ed.* 2018, **57**, 1888.

23 J. Jin, Y. Zheng, S.-z. Huang, P.-p. Sun, N. Srikanth, L. B. Kong, Q. Yan, K. Zhou, *J. Mater. Chem. A* 2019, **7**, 783.

24 H. Yang, Q. Lin, C. Zhang, X. Yu, Z. Cheng, G. Li, Q. Hu, X. Ren, Q. Zhang, J. Liu, C. He, *Nat. Commun.* 2020, **11**, 593.

25 A. J. Bard, L. R. Faulkner, *Electrochemical Methods Fundamentals and Applications*, John Wiley & Sons, Inc., New York 2001, pp. 1– 850.

26 D. Chen, S. D. Minteer, *J. Power Sources* 2015, **284**, 27.

27 G. Chen, Y. Luo, L. Ding, H. Wang, *ACS Catal.* 2018, **8**, 526.